Topological states in amorphous magnetic photonic lattices

Bing Yang,[1,2,*] Hongfang Zhang,[1] Tong Wu,[2] Ruixin Dong,[1] Xunling Yan,[1] and Xiangdong Zhang[2,*]
[1]*School of Physical Science and Information Engineering, Liaocheng University, Liaocheng 252059, China and Shandong Provincial Key Laboratory of Optical Communication Science and Technology, Liaocheng 252059, China*
[2]*Beijing Key Laboratory of Nanophotonics & Ultrafine Optoelectronic Systems, School of Physics, Beijing Institute of Technology, Beijing 100081, China*

(Received 20 November 2018; published 24 January 2019)

Since the discovery of topological phases in optical systems, most of the efforts have been focused on the periodic and quasiperiodic optical structures which have both long-range and short-range orders. In this paper, we construct a kind of two-dimensional aperiodic optical systems, named the amorphous magnetic photonic lattices (AMPLs), which only have short-range orders, and investigate the topological states in these AMPLs. By using the supercell method, we build supercell magnetic photonic crystals as approximate equivalents of the AMPLs. Based on the band structure calculation and full wave simulation, we demonstrate the existence of single-mode and multimode topological edge states in these AMPLs. Through calculating the gapless edge states in reciprocal space, our research gives an intuitive understanding of the topology underlying aperiodic optical systems. Our system provides a platform to explore the relationship between short-range orders and topology and also paves an easy way to fabricate topological optical devices in application.

DOI: 10.1103/PhysRevB.99.045307

I. INTRODUCTION

Since the seminal work of Haldane and Raghu on the topological optical states in two-dimensional (2D) gyroelectric photonic crystals (PCs) [1,2], a great deal of study on the topological phases in PCs and periodically photonic metamaterial systems have been done theoretically and experimentally [3–29]. Analogous to the cases in topological electronic systems [30–32], because of the periodicity, these optical systems may have topological bandgaps and topological edge states (TES) which support robust one-way propagation of light at surfaces of these structures without dissipation. Due to the peculiar properties of the TES, topological optical structures are considered to be very important in potential applications for future photonics and optoelectronics [3,33–37]. Apart from the periodic structures, recent studies have shown that some quasiperiodic photonic lattices and waveguide arrays also have such topological bandgaps and TES [38–42]. In these periodic and quasiperiodic structures, both long-range and short-range orders exist. The topological states in these systems are related to both these orders.

However, for the electronic analogs, only short-range order is necessary for the creation of electron bandgaps as in the amorphous semiconductor structures [43], and recent studies also have proved that topological states can be constructed in electronic and mechanical amorphous systems [44,45]. So our question is, what is the relationship between topological optical states and amorphous optical systems, and can we construct topological states in amorphous optical systems that arise naturally? Although there has been some research on topologically trivial bandgaps in amorphous optical systems [46–49], and on creations and transitions of topological states in disordered optical lattices [50–52], to our knowledge, there has been little discussion on topological states in amorphous optical systems, up to now [53].

In this paper, we construct 2D amorphous magnetic photonic lattices (AMPLs) that only have short-range orders and employ the supercell method and full wave simulation to study their topological properties. Before proceeding, we take particular note of the recent related work by Mansha and Chong [53]. In their studies, they constructed the 2D amorphous photonic lattice using closing-packing algorithm and performed transmission calculations to demonstrate existence of the TES. In contrast, in our studies not only the amorphous lattice constructions, but also the research methods are different from those in Ref. [53]. Our studies give an intuitive understanding of the topology underlying aperiodic optical systems through calculating in reciprocal space. And our system provides a platform to explore the relationship between topology and amorphous structures and also paves an easy way to fabricate topological optical devices in applications. The rest of the paper is arranged as follows. In Sec. II, we introduce the theory and method used in our studies. In Sec. III, the numerical results and discussions are presented. A summary is given in Sec. IV.

II. THEORY AND METHOD

We consider 2D AMPLs composed of magnetic rods immersed in air background. The structure is shown schematically in Figs. 1(a)–1(c). It is constructed as follows [46–48]. First, a regular square with side length a_2 is chosen as the unit cell. Four magnetic rods with radii r are placed at corners of the square as shown in Fig. 1(a). Then, a square lattice array

*Corresponding authors: yangbing@lcu.edu.cn, zhangxd@bit.edu.cn

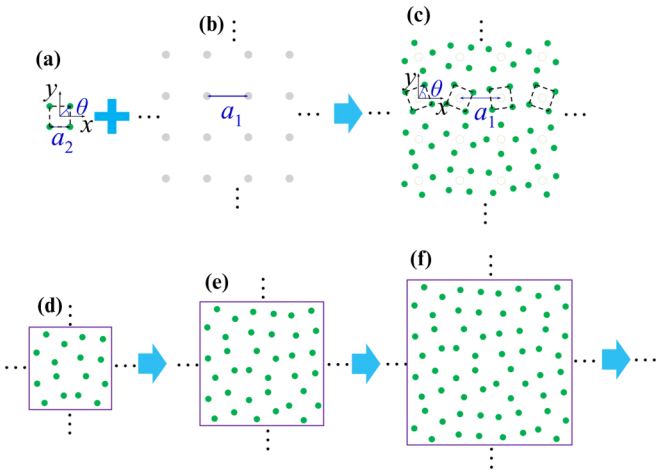

FIG. 1. Structures of the AMPLs and SMPCs. (a) The unit cell with green points denoting magnetic rods. (b) The basic lattice with gray points denoting lattice points. (c) The AMPL. a_1 is the lattice constant of the basic lattice, a_2 and θ are the side length and the randomly rotating angle of unit cell, respectively. (d)–(f) The SMPCs with supercells containing $2 \times 2 = 4$, $3 \times 3, = 9$ and $4 \times 4 = 16$ unit cells, respectively.

with lattice constant $a_1 = 2a_2$ is selected as the basic lattice as shown in Fig. 1(b). Third, we put the unit cells into the lattice array with their geometric centers on lattice points. An AMPL is formed by randomly rotating unit cells against their own centers, i.e., the rotating angle θ is randomly taken for each unit cell as shown in Fig. 1(c). A set of randomly rotating angles correspond to an AMPL configuration. Different AMPL configurations have different detailed structures, but the same short-range order provided by the unit cell [46–48].

When an external dc magnetic field is applied along axes of magnetic rods (z direction), the rods perform strong gyromagnetic anisotropy, with the relative permeability tensor taking the form [4,54,55]

$$\overleftrightarrow{\boldsymbol{\mu}}_r = \begin{bmatrix} \mu_r & i\kappa_r & 0 \\ -i\kappa_r & \mu_r & 0 \\ 0 & 0 & 1 \end{bmatrix}, \tag{1}$$

where μ_r and κ_r are determined by rod components, mode frequency, and external magnetic field. Here, for simplicity, we neglect effects of material dispersion and loss, assuming a constant permeability tensor with real-valued μ_r and κ_r for a particular external magnetic field [4,6]. The relative permittivity of rod is denoted by ε_r, and permeability and permittivity of the air background take values of μ_0 and ε_0 as in vacuum, respectively.

For such AMPLs, we employ the supercell method [52,56] to study their topological properties. By choosing several adjacent unit cells in an AMPL as a supercell, we can build a supercell magnetic photonic crystal (SMPC). Gradually increasing sizes of the supercells as shown in Figs. 1(d)–1(f), in which the supercells contain $2 \times 2 = 4$, $3 \times 3 = 9$ and $4 \times 4 = 16$ unit cells respectively, we can regard the SMPC as an approximate equivalent of the AMPL when the supercell is large enough. Thus, the topological states of the AMPLs can be obtained by studying the topological properties of the SMPCs. It is obvious that larger supercells produce better approximations and when the supercell is infinite, the SMPC is completely equivalent to the AMPL. Based on the bulk-boundary correspondence theorem [4,15,57], through calculating the band structures and the projected edge band diagrams, we can get the topological states of the SMPCs, and hence reveal the topological properties of the corresponding AMPLs. In our studies, we enlarge the supercells gradually as shown in Figs. 1(d)–1(f). Actually, when the supercell contains $4 \times 4 = 16$ unit cells, we think it is sufficient to get the topological properties of the AMPLs through the constructed SMPCs. Here we note that only TM modes with the electric field parallel to the rod axes are considered in our studies [4,15].

III. NUMERICAL RESULTS AND DISCUSSIONS

A. Single-mode topological edge states in AMPLs

Topological states always manifest themselves as robust one-way propagations of TES in 2D structures [1–3,33–37]. In this section, we first construct the single-mode TES, and then in the next section, we investigate the multimode TES in 2D AMPLs. Here, the parameters of the AMPL examples are taken as $a_1 = 2.6\,\text{cm}$, $a_2 = 1.3\,\text{cm}$, $r = 0.2\,\text{cm}$, $\mu_r = 1$, $\kappa_r = 0.4$, and $\varepsilon_r = 15$ [15]. Using the supercell method, we first chose small supercells containing $2 \times 2 = 4$ unit cells as shown in Fig. 1(d) to build SMPCs with each unit cell taking a randomly rotating angle θ. A set of four randomly rotating angles construct a supercell structure, and such a supercell constructs a SMPC configuration. For a concrete AMPL, we calculate tens of different SMPC configurations. In Fig. 2, we only show band structures of four random selections of these tens of SMPCs, with sky blue bars denoting passband ranges and white regions denoting bandgap ranges. Here, we note that due to the lack of the rotational symmetry in SMPCs, we must calculate band structures in the whole first Brillouin zone to get passband and bandgap information. Nevertheless, for our needs and clearer illustration, in Fig. 2, we only show the frequency ranges of passbands and bandgaps in vertical

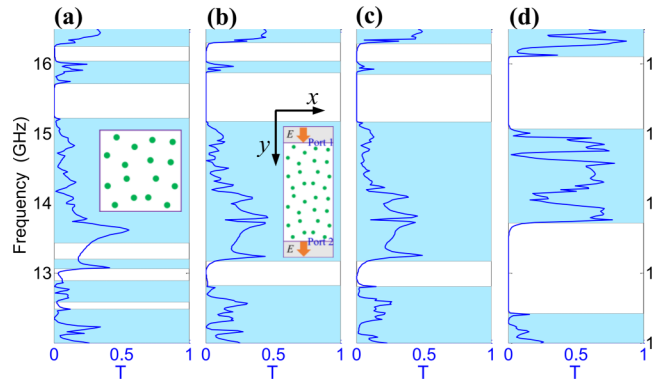

FIG. 2. Band structures of four different SMPCs and transmission coefficients of the corresponding SMPC ribbons. The supercells contain $2 \times 2 = 4$ unit cells. Sky blue bars: passbands, white bars: bandgaps, blue lines: transmission coefficients. Inset in (a) is a supercell sketch and inset in (b) is the calculation model for transmission coefficients in COMSOL multiphysics.

axes. The widths of these bars along horizontal axes have no physical meaning. It can be seen from Fig. 2 that all four of the SMPCs have bandgaps within the frequency range from 12 to 16.5 GHz. An interesting fact is that all the four SMPCs always have two bandgaps around frequencies at 15.5 and 13 GHz, although the details of these bandgaps are different for different SMPC configurations.

We also calculate the transmission coefficients of the ribbon structures for the four SMPCs based on the finite element method (FEM). The calculation model is shown as in the inset in Fig. 2(b) in which the ribbons contain two supercells in the y direction and are periodic in the x direction with light incident at port 1 along the positive y direction. We calculate the scattering coefficients $S_{2,1}$ at port 2. The transmission coefficients $T = |S_{2,1}|$ of the ribbons are shown in the corresponding panels in Fig. 2 with blue curves. It is clear that corresponding to the bandgaps of the SMPCs, the transmission coefficients take minimum values, which confirm the band structures of the SMPCs. Due to the randomness of the rotating angles θ of the unit cells in the SMPCs, the transmission coefficient T has little relation to the direction of incident light [46]. For each SMPC configuration in Fig. 2, we only need to calculate the model once to obtain T.

Then, for studying the topological properties of these SMPCs, in Figs. 3(a)–3(d) we plot the projected edge band diagrams when they are interfaced with metallic boundaries [4,15]. The sky blue areas are projected bulk bands, and the red lines and blue lines are gapless edge states. These gapless edge states are topologically protected and are called TES. Clearly, in all the interfaced SMPC configurations, TES always exist within the frequency ranges corresponding to the bandgaps in Fig. 2. According to the bulk-boundary correspondence theorem [4,15,57], the numbers and slopes of the TES determine the topological invariants of the bandgaps in the corresponding SMPCs. Therefore, the bandgaps near frequencies at 15.5 and 13 GHz in Fig. 2 are topologically nontrivial with Chern numbers $+1$ and -1, respectively. Here we note that due to the periodicity in the horizontal axis k_x, in each bandgap in Figs. 3(a)–3(d), only one TES exists at a single frequency, although there are several line segments in some bandgaps. Also we must note that, for simplicity and clarity, in both Figs. 2 and 3(a)–3(d), we only plot the relatively large bandgaps around frequencies at 15.5 and 13 GHz, although some relatively small bandgaps also exist there, especially around the frequency at 13 GHz. This sort of neglect has no influence on our main results.

To demonstrate these TES more clearly, by using the method in Ref. [51], we first calculate the parameter C_s to show the edge confinement of the electromagnetic (EM) wave, with the model shown in Fig. 3(g) [Fig. 3(h)] in which the SMPS is interfaced with the metallic boundary denoted by a black bold line and the EM radiation is excited by a point source denoted by a violet star near the boundary. The C_s is defined as

$$C_s = \frac{\int_{\Pi_s} \Omega(x,y)dxdy}{\int_{\Pi} \Omega(x,y)dxdy} \tag{2}$$

with $\Omega(xy)$ being the EM energy density at a certain frequency, Π is the whole area of the SMPC under metallic boundary, and Π_s is the interface area with a distance of a_1 away from the metallic boundary. $C_s = 1$ denotes the well-defined edge states. The results of C_s for the case of Fig. 3(a) are shown in Fig. 3(e). Obviously, corresponding to the frequency ranges where the TES locate, most of the EM energies are confined in the interface area Π_s. Due to the narrow widths of the bandgaps, the edge states may leak into the bulk SMPC, leading to the degradation of the edge confinement and the decreasing of C_s from one. Then, in Fig. 3(f), we plot the isolation ratio $R_{AB} = \Omega_A/\Omega_B$ to show the unidirectionality of these TES, with Ω_A, Ω_B being the energy density measured at points A and B, respectively as shown in Fig. 3(g) [Fig. 3(h)]. Point A is on the left and point B is on the right of the source, both with $5a_1$ from the source and $a_1/4$ from the metallic boundary. From Fig. 3(f), we can see the one-way propagations of the EM waves at the interface within the frequency ranges where the TES exist. For the other three SMPC configurations in Figs. 3(b)–3(d), we also perform the same calculations for C_s and R_{AB}. The results are shown in the Supplemental Material [58] and the same conclusions can be obtained. In addition, by using full-wave simulations based on the FEM (COMSOL Multiphysics), we simulate the

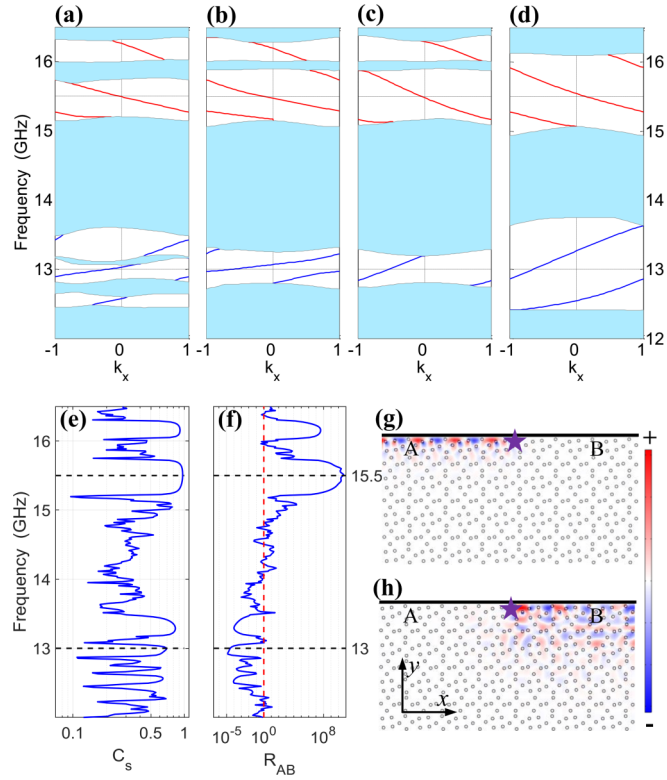

FIG. 3. (a)–(d) TES (blue lines and red lines) in the projected edge band diagrams corresponding to the SMPCs in Figs. 2(a)–2(d), respectively. k_x is normalized with respect to $\pi/(2a_1)$, with $2a_1$ the length of the supercell. Sky blue areas are projected bulk bands. (e), (f) Parameter C_s and isolation ratio R_{AB} for the SMPC configuration in (a), respectively. (g), (h) One-way waveguide propagation field profiles at edges of the SMPC configuration of (a) interfaced on the top with a metallic boundary. Point sources are denoted by violet stars with frequencies at 15.5 and 13 GHz, respectively. Metallic boundaries are denoted by black bold lines.

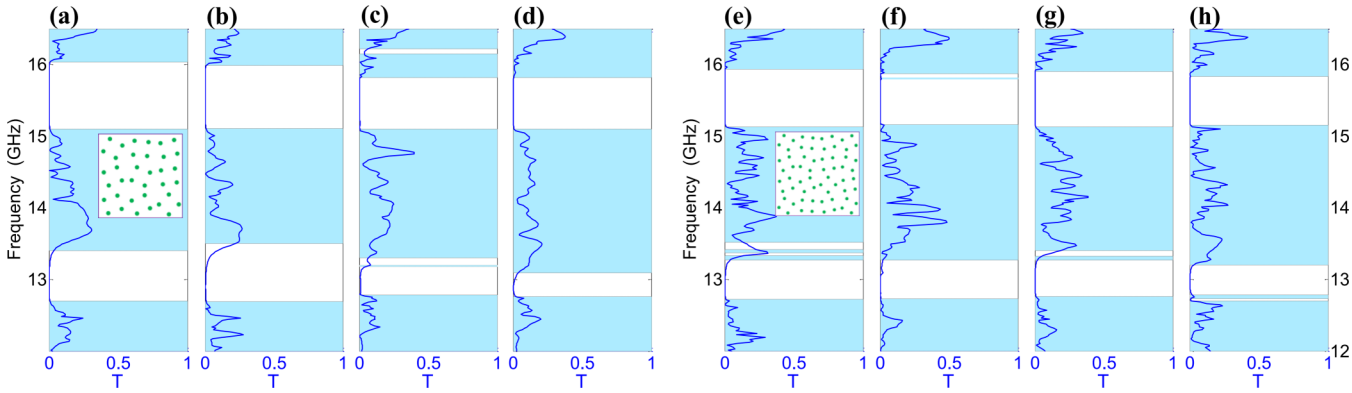

FIG. 4. Band structures of four different SMPCs and transmission coefficients of the corresponding SMPC ribbons. The supercells in (a)–(d) and (e)–(h) contain $3 \times 3 = 9$ and $4 \times 4 = 16$ unit cells, respectively. Sky blue bars: passbands, white bars: bandgaps, blue lines: transmission coefficients. Insets in (a) and (e) are corresponding supercell sketches for two cases, respectively.

one-way waveguide propagations of TES in Fig. 3(a). The results are shown in Figs. 3(g) and 3(h) with frequencies of point sources at 15.5 and 13 GHz, respectively. In Fig. 3(g), the EM wave radiation excited by the point source only propagates to the left without backscattering, while in Fig. 3(h), the EM wave only prorogates to the right without backscattering. In the Supplemental Material [58], we also simulate the robustness of these one-way propagations as they meet with obstacles and defects. All the calculations and simulations confirm the topological properties of these TES.

Then we expand the supercells to contain $3 \times 3 = 9$ and $4 \times 4 = 16$ unit cells, respectively. Also we calculate the band structures and transmission coefficients T of tens of different SMPC configurations for both cases. The randomly selected four results for these two kinds of SMPCs are shown in Figs. 4(a)–4(d) and Figs. 4(e)–4(h), respectively. In calculations of the transmission coefficients T, the similar ribbon models as shown as the inset in Fig. 2(b) is used, just with different unit cells in it. From Fig. 4 we can see that the two main bandgaps near frequencies at 15.5 and 13 GHz also always exist in all SMPCs, although the details are different for different SMPC configurations in both cases.

Correspondingly, in Figs. 5(a)–5(d) and Figs. 5(e)–5(h), we plot the projected edge band diagrams when the SMPCs in Figs. 4(a)–4(d) and Figs. 4(e)–4(h) are interfaced with metallic boundaries, respectively. Clearly, in all these SMPC configurations, gapless TES (red lines and blue lines near the frequencies at 15.5 and 13 GHz) appear within the frequency ranges corresponding to the bandgaps in Fig. 4. Moreover, the numbers and slopes of the TES take the same values as those in Fig. 3, respectively. The results indicate that these TES possess the same topological properties as those in Fig. 3. Also, in the band structures and projected band diagrams in Figs. 4 and 5, we only plot the main bandgaps and neglect the very small bandgaps as in Figs. 2 and 3.

The parameters C_s and isolation ratios R_{AB} are shown in Figs. 5(i) and 5(j) for the SMPC configuration in Fig. 5(a), and in Figs. 5(m) and 5(n) for the SMPC configuration in Fig. 5(e), respectively. The corresponding calculation models are shown in Figs. 5(k) and 5(o), respectively, with the same parameters setting of Π_s, Π, A, and B as we take in Fig. 3(g). Obviously, we can see the edge confinements and the one-way propagations of the EM waves at the interface within the frequency ranges where the TES exist in these figures. For the other SMPC configurations in Figs. 5(b)–5(d) and Figs. 5(f)–5(h), we perform the same calculations in the Supplemental Material [58]. The results show that the similar TES can be obtained near frequencies at 15.5 and 13 GHz in these different SMPC configurations. In Figs. 5(k) and 5(l) and Figs. 5(o) and 5(p), using the full wave simulations, we show the one-way waveguide propagations of the TES in Figs. 5(a) and 5(e), respectively. Point sources are denoted by violet stars with frequencies of 15.5 GHz in Figs. 5(k) and 5(o) and 13 GHz in Figs. 5(l) and 5(p), respectively. Also, as with the simulations in Figs. 3(g) and 3(h), these one-way propagations of the TES are topologically protected due to their nontrivial topology.

From Figs. 2 –5, the following conclusions can be summarized. First, as the sizes of supercells increase, the two main topological bandgaps near the frequencies at 15.5 and 13 GHz always exist in all SMPC configurations. Second, along with the enlarging of supercells, the frequency ranges of these two bandgaps become more and more stable, that is, the selections of the SMPC configurations have less and less influence on these bandgaps and their topologies. Thus, based on these conclusions, we can deduce that as the supercell increases continually, even to the infinite size, which is the same as the case of AMPL, and these two topological bandgaps and the corresponding TES will still be there. These facts ensure that, in our studies, when the supercells increase to contain $4 \times 4 = 16$ unit cells, the corresponding SMPCs can be regarded as good equivalents of the AMPLs for studying their topological properties. In the Supplemental Material [58], we calculate the radical distribution function [46] for these different supercell lattices. The results quantitatively demonstrate that as the supercell grows to contain $4 \times 4 = 16$ unit cells, the SMPCs only have short-range orders, denoting their equivalence to the AMPCs.

In addition, comparing the topological bandgaps in Figs. 2 and 4 with the TES in Figs. 3 and 5, respectively, we can find that in general, the frequency ranges of the TES are slightly larger than those of the corresponding bandgaps. This can be understood as follows. At the edges of the bandgaps, there exist some isolated and narrow bulk bands. These bands

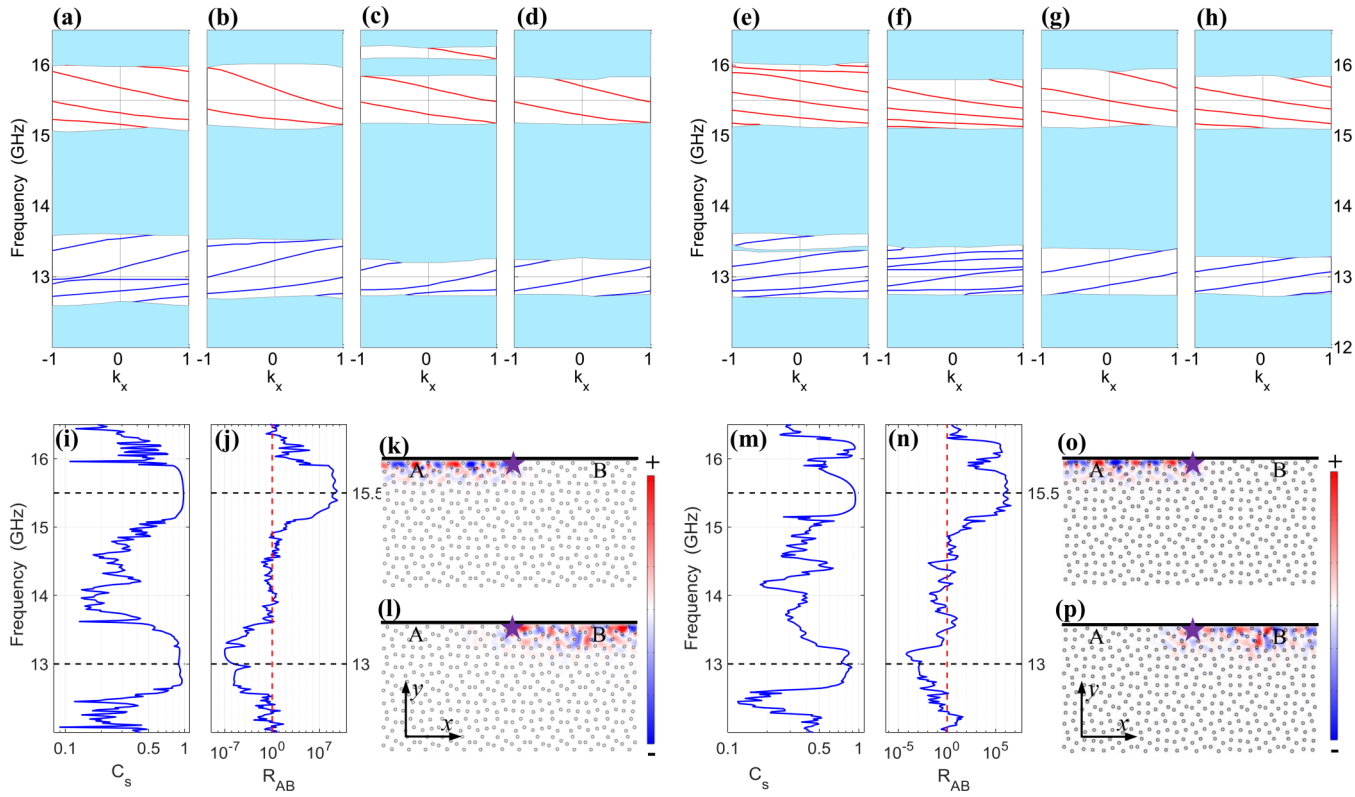

FIG. 5. (a)–(d), (e)–(h) TES (blue lines and red lines) in the projected edge band diagrams corresponding to the SMPCs in Figs. 4(a)–4(d) and Figs. 4(e)–4(h), respectively. k_x is normalized with respect to $\pi/(3a_1)$ in (a)–(d) and $\pi/(4a_1)$ in (e)–(f). (i), (j) C_s and R_{AB} for SMPC in (a); (m), (n) C_s and R_{AB} for SMPC in (e), respectively. (k), (l) and, (o), (p) One-way waveguide propagation field profiles at edges of the SMPCs in (a) and (e) interfaced on the top with metallic boundaries, respectively. Point sources are denoted by violet stars with frequencies at 15.5 GHz in (k), (o) and 13 GHz in (l), (p). Metallic boundaries are denoted by black bold lines.

contribute little to the EM wave propagation in the SMPCs bulk, just as in the case of mobility gaps in topological Anderson insulators in disordered electronic systems [59,60]. At the edges of the mobility gaps, the isolated and narrow bands can localize the electrons and prevent them from transmitting to the inside of the bulks. Thus, these narrow bands in SMPCs will be included into the edge states when the SMPCs are terminated by metallic boundaries, leading to the enlarging of the frequency ranges of the TES in our studies.

B. Multimode topological edge states in AMPLs

The above examples certify that in AMPLs, there can be constructed topological bandgaps with Chern numbers ± 1, corresponding to the single-mode TES. Actually, through tuning the structures and parameters, topological bandgaps with high Chern numbers, corresponding to the multimode TES, also can be constructed in AMPLs. Here we choose the parameters of the AMPLs shown in Fig. 1 as $a_1 = 3.52\,\text{cm}$, $a_2 = 1.76\,\text{cm}$, and $r = 0.22\,\text{cm}$. Other optical parameters of the rods and the air background take values as those in Fig. 2 [15]. Using the methods and procedures as in the study of the above examples, we build corresponding SMPCs and calculate their band structures and TES. Figures 6(a)–6(d) show the projected edge band diagrams of four random selections of tens of different SMPC configurations when the supercells contain $4 \times 4 = 16$ unit cells. It can be seen that near the frequency at 14.5 GHz, all the SMPC configurations have two TES denoted by black lines and red lines. The frequency ranges of the corresponding bandgaps in these four SMPCs are listed in Table I. Also the frequency ranges of the multimode TES are slightly larger than those of the corresponding bandgaps.

According to the bulk-boundary corresponding theorem [4,15,57], these bandgaps are topologically nontrivial with Chern numbers $+2$ and there exist two one-way propagation edge states at the boundaries of the SMPCs near the frequency at 14.5 GHz. To demonstrate these results, in Figs. 6(e)–6(g), we simulate the propagations of the EM waves excited by point sources in different interface waveguides constructed by cladding different square magnetic photonic crystals (MPCs) on the boundary of the SMPC in Fig. 6(a). The point sources are denoted by violet stars with frequencies of 14.5 GHz. The MPCs in Figs. 6(e)–6(g) have topological bandgaps with Chern numbers $+1$, $+2$ and $+3$ near the frequency at

TABLE I. Bandgaps of the four SMPCs in GHz.

	(a)	(b)	(c)	(d)
Top edge	14.741	14.621	14.735	14.692
Bottom edge	14.259	14.282	14.265	14.275

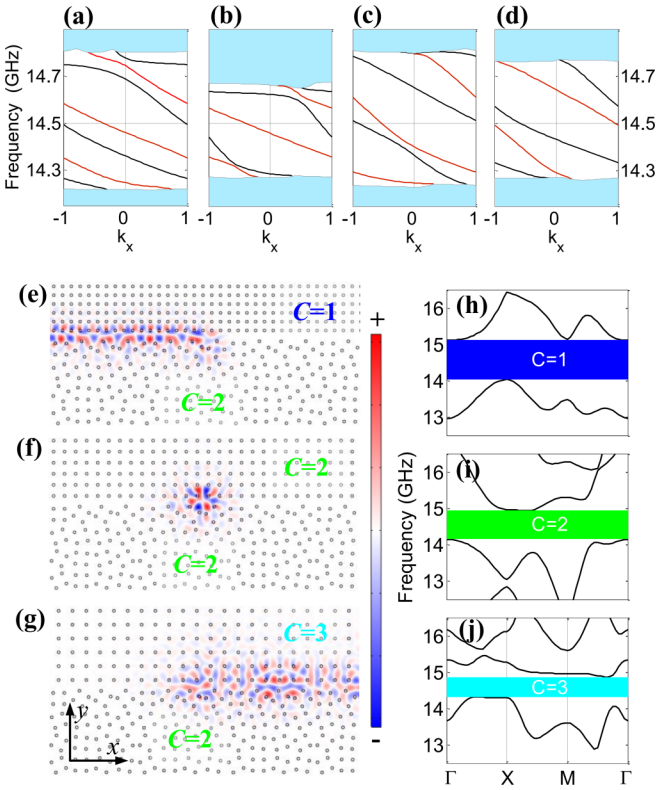

FIG. 6. (a)–(d) TES (red lines and black lines) in the projected edge band diagrams of four SMPC configurations with supercells containing $4 \times 4 = 16$ unit cells. Here $a_1 = 3.52\,\text{cm}$, $a_2 = 1.76\,\text{cm}$ and $r = 0.22\,\text{cm}$. k_x is normalized with respect to $\pi/(4a_1)$. (e)–(g) One-way waveguide propagation field profiles in different interface waveguides constructed by cladding MPCs on the boundaries of the SMPC in (a). Point sources are denoted by violet stars with frequencies at 14.5 GHz. (h)–(j) Band diagrams near frequency at 14.5 GHz for MPCs in (e)–(g), respectively. Topological bandgaps are denoted by color bars marked with Chern numbers.

14.5 GHz as shown in Figs. 6(h)–6(j), respectively [15]. Here the lattice constant a, rod radius r' and gyromagnetic strength $\kappa_{r'}$ of the MPCs take values as $a = 1.39\,\text{cm}$, $r' = 0.214\,\text{cm}$, and $\kappa_{r'} = 0.4$ in Fig. 6(h); $a = 1.76\,\text{cm}$, $r' = 0.22\,\text{cm}$, and $\kappa_{r'} = 0.4$ in Fig. 6(i); $a = 2.19\,\text{cm}$, $r' = 0.219\,\text{cm}$ and $\kappa_{r'} = 0.45$ in Fig. 6(j). The relative permittivity of all rods is 15. Thus, the interface waveguides in Figs. 6(e)–6(g) support TES with Chern numbers $+1$, 0 and -1, respectively. Positive (negative) Chern number denotes the left (right) one-way propagation of the edge state. The zero Chern number denotes the trivial topology of the interface and the localization of the EM wave. Simulation results in Figs. 6(e)–6(g) accord well with our analyses and confirm the existence of multimode TES in the SMPCs. For the other three SMPC configurations in Figs. 6(b)–6(d), we also perform the same simulations in the Supplemental Material [58] and obtain the same results.

We also study the cases of the supercells containing $2 \times 2 = 4$ and $3 \times 3 = 9$ unit cells. Similar characteristics as we have got from the examples in Figs. 2 –5 have been obtained (not shown here). Thus, we deduce these TES in Figs. 6(a)–6(d) will still stay there as the sizes of supercells increase continually, showing that in AMPLs, topological states with high Chern numbers also can be constructed.

IV. SUMMARY

In this paper, we constructed aperiodic AMPLs which only have short-range orders and studied their topological properties. Using the supercell method, we built SMPCs that are approximately equivalent to the studied AMPLs by gradually increasing sizes of the supercells. Through checking the topological bandgaps and TES in the SMPCs, we obtained the topological properties of the AMPLs. The results show that by tuning the structures and parameters, single-mode and multimode TES also can be constructed in aperiodic optical structures of AMPLs. By calculating the gapless edge states in reciprocal space, our research gives an intuitive understanding of the topology underlying aperiodic optical systems, such as comprehending topology in periodic optical systems [1,4,15]. Our system provides a platform to explore the relationship between short-range orders and topology. And, due to the easy fabrications of the amorphous optical structures, our study also paves an easy way to manufacture topological optical devices in application.

ACKNOWLEDGMENTS

We thank COMSOL Co., Ltd. for their trial version of COMSOL 5.3. This work is supported by the National Key R&D program of China (Grant No. 2017YFA0303800), the National Natural Science Foundation of China (Grants No. 61421001 and No. 61574071), the Research Fund from the MOE of China (Grant No. JZW17SL01), the Natural Science Foundation of Shandong Province (Grant No. ZR2018MA036), and Liaocheng University (Grant No. 318051705).

[1] F. D. M. Haldane and S. Raghu, Phys. Rev. Lett. **100**, 013904 (2008).
[2] S. Raghu and F. D. M. Haldane, Phys. Rev. A **78**, 033834 (2008).
[3] T. Ozawa, H. M. Price, A. Amo, N. Goldman, M. Hafezi, L. Lu, M. Rechtsman, D. Schuster, J. Simon, O. Zilberberg, and I. Carusotto, Rev. Mod. Phys. (to be published).
[4] Z. Wang, Y. D. Chong, J. D. Joannopoulos, and M. Soljačić, Phys. Rev. Lett. **100**, 013905 (2008).
[5] Z. Wang, Y. D. Chong, J. D. Joannopoulos, and M. Soljačić, Nature (London) **461**, 772 (2009).
[6] T. Ochiai and M. Onoda, Phys. Rev. B **80**, 155103 (2009).
[7] C. He, X. L. Chen, M. H. Lu, X. F. Li, W. W. Wan, X. S. Qian, R. C. Yin, and Y. F. Chen, Appl. Phys. Lett. **96**, 111111 (2010).
[8] K. Fang, Z. Yu, and S. Fan, Phys. Rev. B **84**, 075477 (2011).
[9] M. Hafezi, E. A. Demler, M. D. Lukin, and J. M. Taylor, Nat. Phys. **7**, 907 (2011).
[10] K. Liu, L. Shen, and S. He, Opt. Lett. **37**, 4110 (2012).

[11] A. A. Asatryan, L. C. Botten, K. Fang, S. Fan, and R. C. McPhedran, Phys. Rev. B **88**, 035127 (2013).

[12] M. Hafezi, S. Mittal, J. Fan, A. Migdall, and J. Taylor, Nat. Photon. **7**, 1001 (2013).

[13] A. B. Khanikaev, S. Hossein Mousavi, W.-K. Tse, M. Kargarian, A. H. MacDonald, and G. Shvets, Nat. Mater. **12**, 233 (2013).

[14] M. C. Rechtsman, J. M. Zeuner, Y. Plotnik, Y. Lumer, D. Podolsky, F. Dreisow, S. Nolte, M. Segev, and A.Szameit, Nature (London) **496**, 196 (2013).

[15] S. A. Skirlo, L. Lu, and M. Soljačić, Phys. Rev. Lett. **113**, 113904 (2014).

[16] S. A. Skirlo, L. Lu, Y. Igarashi, Q. Yan, J. Joannopoulos, and M. Soljačić, Phys. Rev. Lett. **115**, 253901 (2015).

[17] T. Ma, A. B. Khanikaev, S. H. Mousavi, and G. Shvets, Phys. Rev. Lett. **114**, 127401 (2015).

[18] L. H. Wu and X. Hu, Phys. Rev. Lett. **114**, 223901 (2015).

[19] C. He, X. C. Sun, X. P. Liu, M. H. Lu, Y. Chen, L. Feng, and Y.-F. Chen, Proc. Natl. Acad. Sci. USA **113**, 4924 (2016).

[20] X. Cheng, C. Jouvaud, X. Ni, S. H. Mousavi, A. Z. Genack, and A. B. Khanikaev, Nat. Mater. **15**, 542 (2016).

[21] B. Xiao, K. Lai, Y. Yu, T. Ma, G. Shvets, and S. M. Anlage, Phys. Rev. B **94**, 195427 (2016).

[22] L. Lu, C. Fang, L. Fu, S. G. Johnson, J. D. Joannopoulos, and M. Soljačić, Nat. Phys. **12**, 337 (2016).

[23] F. Gao, H. Xue, Z. Yang, K. Lai, Y. Yu, X. Lin, Y. Chong, G. Shvets, and B. Zhang, Nat. Phys. **14**, 140 (2017).

[24] B. Yang, T. Wu, and X. Zhang, Appl. Phys. Lett. **110**, 021109 (2017).

[25] B. Yang, T. Wu, and X. Zhang, J. Opt. Soc. Am. B **34**, 831 (2017).

[26] Y. Yang, Y. F. Xu, T. Xu, H. X. Wang, J. H. Jiang, X. Hu, and Z. H. Hang, Phys. Rev. Lett. **120**, 217401 (2018).

[27] Q. Yan, R. Liu, Z. Yan, B. Liu, H. Chen, Z. Wang, and L. Lu, Nat. Phys. **14**, 461 (2018).

[28] F. Liu, H. Y. Deng, and K. Wakabayashi, Phys. Rev. B **97**, 035442 (2018).

[29] B. Y. Xie, H. F. Wang, H. X. Wang, X. Y. Zhu, J. H. Jiang, M. H. Lu, and Y. F. Chen, Phys. Rev. B **98**, 205147 (2018).

[30] M. Z. Hasan and C. L. Kane, Rev. Mod. Phys. **82**, 3045 (2010).

[31] X. L. Qi and S. C. Zhang, Rev. Mod. Phys. **83**, 1057 (2011).

[32] A. Bansil, H. Lin, and T. Das, Rev. Mod. Phys. **88**, 021004 (2016).

[33] L. Lu, J. D. Joannopoulos, and M. Soljačić, Nat. Photon. **8**, 821 (2014).

[34] L. Lu, J. D. Joannopoulos, and M. Soljačić, Nat. Phys. **12**, 626 (2016).

[35] A. B. Khanikaev and G. Shvets, Nat. Photon. **11**, 763 (2017).

[36] X. C. Sun, C. He, X. P. Liu, M. H. Lu, S. N. Zhu, and Y. F. Chen, Prog. Quant. Electr. **55**, 52 (2017).

[37] B. Y. Xie, H. F. Wang, X. Y. Zhu, M. H. Lu, Z. D. Wang, and Y. F. Chen, Opt. Express **26**, 24531 (2018).

[38] Y. E. Kraus, Y. Lahini, Z. Ringel, M. Verbin, and O. Zilberberg, Phys. Rev. Lett. **109**, 106402 (2012).

[39] M. Verbin, O. Zilberberg, Y. E. Kraus, Y. Lahini, and Y. Silberberg, Phys. Rev. Lett. **110**, 076403 (2013).

[40] Y. E. Kraus, Z. Ringel, and O. Zilberberg, Phys. Rev. Lett. **111**, 226401 (2013).

[41] M. Verbin, O. Zilberberg, Y. Lahini, Y. E. Kraus, and Y. Silberberg, Phys. Rev. B **91**, 064201 (2015).

[42] M. A. Bandres, M. C. Rechtsman, and M. Segev, Phys. Rev. X **6**, 011016 (2016).

[43] M. Kastner, Phys. Rev. Lett. **28**, 355 (1972).

[44] N. P. Mitchell, L. M. Nash, D. Hexner, A. M. Turner, and W. T. Irvine, Nat. Phys. **14**, 380 (2018).

[45] A. Agarwala and V. B. Shenoy, Phys. Rev. Lett. **118**, 236402 (2017).

[46] C. Jin, X. Meng, B. Cheng, Z. Li, and D. Zhang, Phys. Rev. B **63**, 195107 (2001).

[47] Y. Wang, B. Cheng, and D. Zhang, Appl. Phys. Lett **83**, 2100 (2003).

[48] Y. Wang and S. Jian, Phys. Lett. A **352**, 550 (2006).

[49] M. Rechtsman, A. Szameit, F. Dreisow, M. Heinrich, R. Keil, S. Nolte, and M. Segev, Phys. Rev. Lett. **106**, 193904 (2011).

[50] P. Titum, N. H. Lindner, M. C. Rechtsman, and G. Refael, Phys. Rev. Lett. **114**, 056801 (2015).

[51] C. Liu, W. Gao, B. Yang, and S. Zhang, Phys. Rev. Lett. **119**, 183901 (2017).

[52] M. Xiao and S. Fan, Phys. Rev. B **96**, 100202 (2017).

[53] S. Mansha and Y. D. Chong, Phys. Rev. B **96**, 121405 (2017).

[54] J. Lian, J. X. Fu, L. Gan, and Z. Y. Li, Phys. Rev. B **85**, 125108 (2012).

[55] S. T. Chui, S. Liu, and Z. Lin, Phys. Rev. E **88**, 031201 (2013).

[56] Z. Y. Li, X. Zhang, and Z. Q. Zhang, Phys. Rev. B **61**, 15738 (2000).

[57] Y. Hatsugai, Phys. Rev. Lett. **71**, 3697 (1993).

[58] See Supplemental Material at http://link.aps.org/supplemental/10.1103/PhysRevB.99.045307 for the results of C_s and R_{AB}, and radical distribution function for different SMPC configurations, robustness of the one-way propagation of TES and simulation of the multi-mode TES.

[59] J. Li, R. L. Chu, J. K. Jain, and S. Q. Shen, Phys. Rev. Lett. **102**, 136806 (2009).

[60] Y. Y. Zhang, R. L. Chu, F. C. Zhang, and S. Q. Shen, Phys. Rev. B **85**, 035107 (2012).